Optimizing energy conversion in a PV-TGS (mSi-Bi_2Te_3) using numerical simulation of semiconductor materials

D. Fuentes-Hernández[a], M. Vargas-Ramírez[a,*], F. Legorreta-García[a,*], E. U. Morales-Cruz[b], E. A. Chávez-Urbiola[c], and C. Y. Becerra-Mayorga[a]

[a]*Área Académica de Ciencias de la Tierra y Materiales, Instituto de Ciencias Básicas e Ingeniería, Universidad Autónoma del Estado de Hidalgo, Carr. Pachuca-Tulancingo km 45, Carboneras, Mineral de la Reforma, Hidalgo, México.*

[b]*Escuela Superior de Ingeniería Química e Industrias Extractivas, Instituto Politécnico Nacional, Av. Instituto Politécnico Nacional, Lindavista, Gustavo A. Madero, 07700 Ciudad de México, CDMX,*

[c]*Centro de Investigación en Ciencia Aplicada y Tecnología Avanzada-Querétaro, Instituto Politécnico Nacional, Cerro Blanco No. 141 Col. Colinas del Cimatario, 76090, Santiago de Querétaro, Querétaro, México.*

Received 11 July 2025; accepted 25 August 2025

A numerical simulation model based on the energy transfer and conversion by the semiconductor materials of a Photovoltaic-Thermoelectric Generation System (PV-TGS) was developed to determine its theoretical power. The model yielded results that differed from those previously reported by other authors for PV panels and cells by a range of -0.017% to +1.74%. In thermoelectric production, the results deviated by a range of -2.27% to -2.80%. The model was formulated based on the constitutive equations of the phenomena inherent to the photovoltaic generation of a monocrystalline silicon PV panel (mSi) and the thermoelectric generation of bismuth telluride (Bi_2Te_3) Thermoelectric Generators (TEGs). The primary variables of interest were irradiance G, panel operating temperature (T_{PVP}), and the cold section (T_c) of each Thermoelectric Generator (TEG), as well as the generated electrical power P. The research outcomes enabled the identification of the optimal number of TEGs for the design of a PV-TGS. This determination was derived by considering the temperature differential between the T_{PVP} and T_c sections, as well as the generation efficiency of PV-TGS as a function of incident radiation. Consequently, a pair of equations was formulated that establish a direct correlation between the thermoelectric generation rate and the desired output power.

Keywords: Photovoltaic-thermoelectric generation systems; computer simulation; energy transfer; thermoelectric generators; solar hybrid systems.

DOI: https://doi.org/10.31349/RevMexFis.72.011002

1. Introduction

In an effort to reduce greenhouse gas emissions during the generation of electricity for diverse economic and industrial applications, humans have devised numerous environmentally superior technologies. These innovative methods stand in stark contrast to conventional methods that rely on fuels derived from petroleum or other mineral resources [1]. Among these technologies, solar photovoltaic has achieved the greatest development and maturity, enabling its current applications to span from domestic power supplies to production in distribution plants. This advancement has motivated various research projects aimed at enhancing the performance of commercial photovoltaic cells and panels. These investigations encompass a range of approaches, including the implementation of cooling systems to mitigate the impact of operating temperature and the development of reflective surfaces that augment the incidence of radiation, thereby increasing the photogenerated electric current. These advancements have enabled to approach the well-known Shockley-Queisser limit [2,3]. In line with this trend, PV-TGS represents a hybrid solar system designed to capitalize on the residual heat generated during the operation of conventional photovoltaic systems and convert it into a second electrical power output. This transformation is achieved through TEGs, which, utilizing the well-established Seebeck effect, can convert the temperature disparity between their plates into electrical potential. However, for the T_{PPV} panel to be fully functional, the incident radiation must exceed normal operating conditions. Consequently, various investigations have explored the utilization of concentrators and reflectors as an alternative approach. This approach not only enhances the electrical energy generation by the PV panel but also augments the residual heat that can be utilized by thermoelectric devices and encourages the development of cooling systems that maintain the Tc at a suitable level. Nevertheless, current research is confined to constructing various configurations of these systems and characterizing them under realistic operating conditions in diverse geographical locations. Notably, it lacks a prediction of the anticipated electrical power output based on the components incorporated in their construction [4,5]. Computational tools, particularly multiphysics simulation, have demonstrated their efficacy in predicting the behavior of diverse phenomena, processes, and systems. This has led to their widespread adoption in the design of devices and products, spanning from laboratory to commercial and industrial scales. Notably, the elimination of the need for physical prototypes reduces production costs significantly [6-10].

These advantages can also be leveraged in scientific research, as evidenced since the 1960s. Two decades later, computer technology had sufficiently advanced for various public and private initiatives to be commercialized and disseminated. In 1998, [11] conducted studies comparing various software and methodologies in the prediction of solar energy generation. The findings indicated that the prediction of heat transfer was adequate as long as it was performed in a single dimension. However, significant challenges arose when incorporating information from the environment, such as fluctuations in ambient temperature, incident radiation, and the coefficients involved in convection. In a similar manner, [12] developed an alternative model for the design of photovoltaic systems. They began by utilizing the constitutive equations of a photovoltaic cell to construct an equivalent electrical circuit. This model identified irradiance and operating temperature as the most significant variables, which influenced various parameters such as photogenerated current, saturation current, diode characteristics, series connection resistance, parallel connection resistance, voltage, and power output. It was observed that the intensity of irradiance directly correlated with the generated electric current, while an increase in temperature resulted in a proportional rise in photogenerated current, accompanied by a concomitant increase in voltage loss within polycrystalline silicon panels. In recent research conducted in 2010, [13] developed a MATLAB Simulink model, similar to the one described above, to assess the performance of a hybrid photovoltaic thermal system (PV/T). The model demonstrated an error of less than 2% compared to experimental measurements. In 2012, [14] conducted a comparative study of electrical power generation from a monocrystalline silicon photovoltaic panel under various operational conditions, including distinct operating temperatures, irradiance levels, ideality factors, and interconnection resistances, and in collaboration, they developed a simulation model utilizing MATLAB Simulink. Later, in 2015 [15] developed a model and simulated the behavior of a 60-cell 250 W panel under varying irradiance (G) and operating temperature conditions. This simulation was conducted to compare the performance of silicon and germanium cells. The simulations were executed using MATLAB Simulink software. In turn, [16] conducted a theoretical study to assess the impact of the angle of incidence on solar energy generation. The study employed computational simulation in MATLAB to evaluate the effects of the angle of incidence on the generation of solar energy throughout the year. The results indicated that the optimal angle for installing photovoltaic systems in the Baghdad region is 33°, where the highest incident radiation is obtained. In the same year, [17] utilized MATLAB Simulink to develop a simulation of a solar-powered unified power conditioner. This simulation demonstrated the ability to reduce total harmonic distortion by 4.76% in current and 3.86% in voltage in arrays of up to 64 photovoltaic panels. In 2019, [18] developed a block model using MATLAB Simulink that enables the comparison of simulated cell values with data obtained from their physical characterization. This analysis revealed that the discrepancies between simulations and characterizations primarily stem from electrical power losses resulting from the internal resistance of circuits and voltage and temperature fluctuations. As previously discussed, simulation serves as a potent tool in the planning and design of photovoltaic systems, facilitating the accurate prediction of their performance. In 2021, [19] investigated using Finite-Difference Time-Domain (FDTD) simulations how the size and shape of gold nanoparticles influence sunlight absorption in dye-sensitized solar cells (DSSCs) to improve their conversion efficiency. The nanoparticles were modeled in radii ranging from 15 to 85 nm embedded in a 100 nm thick TiO_2 layer. The incidence was varied at angles from 0 to 70°, obtaining that the 85 nm nanoparticles presented the highest plasmonic absorption of wavelengths between 450 and 800 nm at an angle of 70° due to the generation of multiple plasmonic resonances, which broadens the absorption spectrum. In the same year, in Ref. [20] they developed an Interval Type 2 Fuzzy Logic Controller (IT2FLC) for maximum PowerPoint tracking (MPPT) in a TEGs array and compared it with the traditional Perturb and Observe (P&O) algorithm, using MATLAB Simulink software. This resulted in a response time ~ 0.2 s faster than P&O and without oscillations. Based on the simulation data, IT2FLC outperforms P&O in stability, efficiency, and adaptability to load and temperature variations, making its application in hybrid solar systems recommendable. The computational simulation has a wide range of applications beyond analyzing generation systems. It can also be directly applied to studying the phenomena inherent in energy conversion by semiconductor materials and designing these materials. In 2024, [21] conducted a comprehensive numerical analysis of solid-state quantum dot-based hybrid solar cells (SSQDSCs) using SCAPS-1D software. The primary objective of this study was to optimize the performance of the configuration, which included the frontal contact of Fluoride Tin Oxide (FTO), metal oxides (titanium oxide (TiO_2), zinc oxide (ZnO), and tin dioxide (SnO2)), cadmium sulfide (CdS) quantum dots, poly (3-hexylthiophene) (P3HT) hole-transporting and absorbing layer, and platinum (Pt) three-way contact. The study varied parameters such as thickness, electron affinity, interstitial defects, work function, and quantum confinement effects of the CdS dots. Notably, the study determined the efficiency as a function of the semiconductor, with the highest efficiency observed for SnO_2 at 15.15%, followed by ZnO at 14.88% and TiO_2 at 14.7%. In contrast, [22] they made a theoretical study on the structural, electronic, and optical characteristics of MA_2GeI_4 (MA = methylammonium, CH_3NH_3), a lead (Pb)-free two-dimensional perovskite material suitable for solar cell absorbers. To achieve this, they employed a combination of density functional theory (DFT) and the spectrally limited maximum efficiency (SLME) model, utilizing the Quantum ESPRESSO software. Consequently, they determined that the material's band gap of 1.37 eV makes it an optimal candidate for absorbing sunlight, resulting in a theoretical conversion efficiency of 32.6%, which closely approximates the

Shockley-Queisser limit. In this same year, [23] published a computational study that combined DFT and Boltzmann transport theory to analyze half-Heusler (hH) alloys as potential candidates for high-temperature thermoelectric generators. The study utilized Quantum ESPRESSO to evaluate the performance of TiPtPb compounds, which were compared to other TiXPb compounds (X = Ni, Pb, Pt). Khatri's findings revealed that TiPtPb compounds exhibited exceptional properties, including low lattice thermal conductivity and high-power factor, setting them apart from their counterparts. This theoretical study serves as a foundation for the development of semiconductor materials for high temperatures, addressing the limitations of commercial alternatives. As a consequence of this research, a simulation model was developed that, unlike the previously mentioned models, not only visualizes the photovoltaic cell as an electrical circuit but also incorporates the construction materials and the phenomena associated with energy conversion, whose substantial implications are responsible for its electrical power output. Furthermore, the same simulation model incorporates the effects of panel temperature on the thermoelectric generation of TEGs, which, when combined, facilitate the utilization of residual heat and augment the generation of electrical energy.

2. Methodology

Figure 1 presents a comprehensive overview of the experimental procedure devised for the simulation of the PV-TGS. Each stage of the procedure is detailed below.

2.1. PV panel simulation

For the simulation's development, the *Solar Cell* application was utilized within the semiconductor module of the Comsol Multiphysics software considering as cell material mSi [24-25].

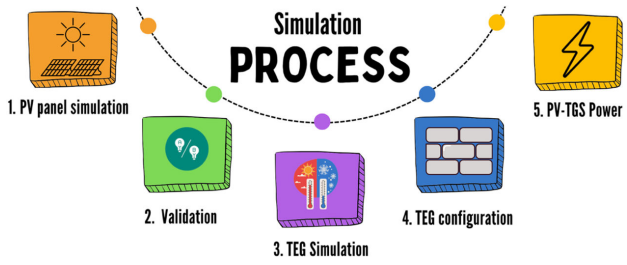

FIGURE 1. PV-TGS simulation process. Own elaboration.

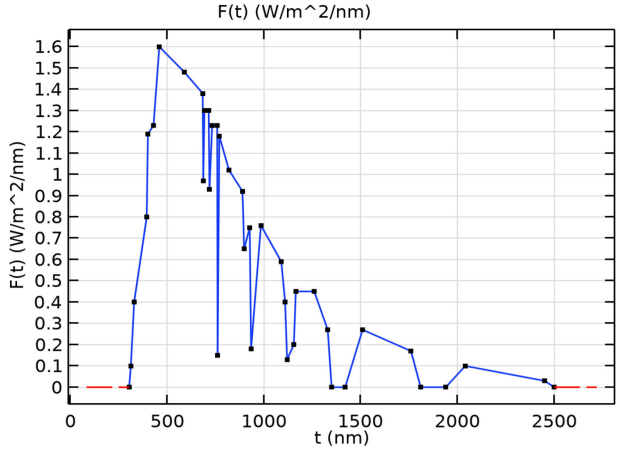

FIGURE 2. ASTM-173-03 Standard: A Comprehensive Overview of the Utilizable Solar Spectrum [24].

2.1.1. *Incident radiation*

The interpolation of solar radiation was conducted based on the spectrum established by the ASTM-173-03 standard [26]. This spectrum was obtained through an approximation incorporated within the simulation module depicted in Fig. 2, whose intensity corresponds to $G = 1000$ W/m^2.

2.1.2. *Absorption function*

The interpolation function was employed to determine the quantity of radiation absorbed by the material and utilized by it to transfer electrons from the valence band to the conduction band. In the case of silicon, this material absorbs radiation from 1.107 eV (approximately equivalent to wavelengths of 1120 nm) up to wavelengths of 400 nm in length [27]. For this purpose, the functions $nref = 1$ (reflectivity index) and $kref = 2$ (excitation coefficient) were designated.

2.1.3. *Geometry*

The cell's geometry is one-dimensional (1D), with a depth of 250 micrometers. This depth is significant because the interactions that generate the photogenerated current occur within a wavelength range of 400 to 1150 nm at a depth between 180 and 200 μm [28]. The total surface area of the cell was 142 cm^2 [29].

TABLE I. Declaration of the variable G_{ph} belonging to photogeneration.

Name	Expression	Unit
G_{ph}	(4*pi/(h_const*c_const)*integrate(kref(lm)*F(lm)*exp(-4*pi*kref(lm)*x/lm), lm,25[nm],1300[nm]))	1/(m^3·s)

Prepared by the authors with data from [25].

2.1.4. Photogeneration (G_{ph}): PV panel generation

Once the incident radiation and the quantity of energy absorbed by the material were determined, the energy that the material can convert into an electric current as a result of the photoelectric effect was calculated. The variable and its declaration are presented in Table I, which is equivalent to Eq. (1) and corresponds to the photogeneration rate as a function of depth z ($G(z)$) into the device from the surface, λ is the wavelength, $\alpha(\lambda)$ is the absorption coefficient rate defined by Eq. (2) where $\kappa(\lambda)$ is the imaginary part of the refractive index, and $\phi(\lambda)$ is the photon generation rate defined by Eq. (3), where $F(\lambda)$ is the spectral irradiance given for the approximation by the AM 1.5 spectrum shown in Fig. 2 [24-26,30], h is Planck's constant (6.626×10^{-34} J·s) and c is the speed of light (3×10^{8} m/s).

$$G(z) = \int_0^{\infty} \alpha(\lambda)\phi(\lambda)\exp(\alpha(\lambda)zd\lambda, \tag{1}$$

$$\alpha\left(\lambda\right) = \frac{4\pi\kappa\left(\lambda\right)}{\lambda}, \tag{2}$$

$$\phi\left(\lambda\right) = \frac{\lambda}{hc}F\left(\lambda\right). \tag{3}$$

2.1.5. Semiconductor material model

The initial equation solved was that of charge carrier density ρ as a function of the relative permittivity of the material ϵ_r and the vacuum permittivity ϵ_0, as well as the applied voltage V, as presented in Eq. (4).

$$\nabla \cdot (-\epsilon_0\epsilon_r\nabla V) = \rho. \tag{4}$$

This subsequently enabled the determination of the quantity of electrons and holes ρ^+ that would generate the photogenerated current. The equations that model the phenomena occurring during the photoelectric effect are presented below. Equation (5) (Poisson's equation) relates the carrier density as a function of the electron charge q to the number of positive or hole p and negative n carriers, as well as the densities of donor and acceptor atomic charges N_d^+ and N_a^-. In this context, both electrons and holes possess the same magnitude of charge, albeit with opposite signs [31].

$$\rho^+ = q\left(p - n + N_d^+ N_a^-\right). \tag{5}$$

In turn, the pair of Eqs. (6) and (7) determined the concentration of positive and negative charges in the depletion region n and its edges γ_n and γ_p as a function of the electronic charge, the work function Ef_0, which is dependent on the material, the charge density in the valence and conduction bands N_v and N_c, and the energies related to the valence E_v and conduction E_C bands. All these variables are affected by the reference temperature T_I, which was determined by the Nasrin equation [32] and is equivalent to the T_{PVP}. In both equations, k_B is the Boltzmann constant.

$$n = N_c\gamma_n \exp\left(\frac{q\left(Ef_0 - E_c\right)}{k_B T_I}\right), \tag{6}$$

$$n = N_v\gamma_p \exp\left(\frac{q\left(E_v - Ef_0\right)}{k_B T_I}\right). \tag{7}$$

Equations (8) and (9) were derived from the conversion of the Poisson equation into flow equations, enabling the calculation of the total current generated along an electrical conductor current density J resulting from the recombination of both types of charges J_n and J_p. Consequently, terms such as mobility μ_n and μ_p and the diffusion capacity of charge carriers $D_{n_{,th}}$ and $D_{p_{,th}}$ were incorporated to determine the generation capacity G_{ph}.

$$\begin{aligned} J_n &= qn\mu_n\nabla E_c + \mu_n k_B T G_{ph}\left(n/N_c\right)\nabla n \\ &\quad + qnD_{n,th}\nabla ln\left(T_I\right), \end{aligned} \tag{8}$$

$$\begin{aligned} J_p &= qp\mu_p\nabla E_V + \mu_p k_B T G_{ph}\left(p/N_V\right)\nabla \mathrm{p} \\ &\quad + qpD_{p,th}\nabla \ln\left(T_I\right). \end{aligned} \tag{9}$$

Consequently, it can be asserted that the first of these (4) describes the electric current generated by the electric field applied to the semiconductor, which flows in the opposite direction to the electric field $Drift$. The second Eq. (5) describes the behavior of hole diffusion on the semiconductor's surface due to the incidence of sunlight and its absorption capacity. The analytical doping Eqs. (10) and geometric doping Eqs. (11), (12), and (13) are employed to determine the number of donor doping atoms N_D and acceptor doping atoms N_A formed during the photoelectric effect. N_A^{prev} represents the concentration of acceptors at the starting time of the simulation. It is noteworthy that if all dopant atoms are ionized, $N_d^+ = N_D$ and $N_a^- = N_A$.

$$N_D = N_D^{\text{prev}} + N_{D0}; N_A = N_A^{\text{prev}}. \tag{10}$$

In the scenario where not all atoms are ionized, the donor concentration will be equivalent to the atoms previously present in the junction zone between the two sections of the doped semiconductor N_D^{prev} and those that remain in a latent state N_{D0}. Conversely, if acceptor atoms become completely ionized, their concentration will equal that of the carriers present in the junction. This non-ionization behavior may be attributed to the absorption depth and/or the wavelength at which the semiconductor interacts. The above depends on the distance from the distribution center r, typically at $r = 0$, the largest number of acceptors is present N_{A0}. By considering the change in charge concentration along the thickness of the material l, it is possible to determine the thickness of the depletion zone l_d as a function of the concentration of electrons and holes and the diffusive flow d_j of the dopants from the depth of the material N_b.

$$N_D = N_D^{\text{prev}}, \tag{11}$$

$$N_A = N_A^{\text{prev}} + N_{A0} \exp\left[-\left(\frac{r}{l_d}\right)^2\right], \tag{12}$$

$$l_d = \frac{d_j}{\sqrt{\ln\left(\frac{N_{A0}}{N_b}\right)}}. \tag{13}$$

To assess the system's response under varying irradiance conditions, simulations were conducted using G values ranging from 1000 to 2000 W/m^2, with increments of 200 W/m^2. This approach ensured that the operating temperature was systematically affected in parallel with the photovoltaic generation.

2.1.6. Meshing

The mesh applied was fine, with a maximum size of 10 nm at the left end, where contact 1 is situated (coordinate 0,0), and smoothing was applied until reaching the contact 2 ends on the right (coordinate 250,0) with 546 elements. The primary objective was to scrutinize the recombination of charge carriers within the semiconductor material as the depth increases.

2.2. Validation of PV panel simulations

To validate the simulation results, a comparative analysis was conducted between the findings of [14,15,18]. These studies focused on the electrical power generated by a PV panel under identical operational conditions. This comparative analysis validated the suitability of the simulation model for predicting photovoltaic energy.

2.3. Simulation TEG

In the TEG simulation, the TGM-127-1.4-2.5 model from Kryotherm was utilized as a reference. The construction materials employed were Bi_2Te_3 doped with positive and negative charges, silver solder, and alumina in the warm and cold sections encapsulating the semiconductor materials and conductive solder. To establish a reference parameter and validate the simulation, the identical temperature differences employed by the manufacturer for its characterization (170, 150, and 120°C) were utilized. Subsequently, simulations were conducted with the PV panel operating temperatures derived from the results of section 2.1.5.

2.3.1. Heat transfer

The heat transfer q between the materials is conducted, necessitating the application of Fourier's law Eq. (15) to determine the variables of interest. This equation is derived from the conservation of energy Eq. (14), where variables include the density ρ, heat capacity at constant pressure C_p, temperature change rate component u, temperature gradient ∇T, the rate of heat generation Q and conduction coefficient k, all of which are intensive properties of the materials. Additionally, the temperature gradient between the warm and cold sections is a crucial factor in this analysis.

$$\rho C_p u \cdot \nabla T + \nabla \cdot q = Q, \tag{14}$$

$$q = -k\nabla T. \tag{15}$$

2.3.2. Electric current

The generated electric current density J is calculated by solving the equations of diffusion current density J_e, which in this case refers to that caused by the Seebeck effect. Therefore, the variables considered were conductivity σ_e, the Seebeck coefficient S. Which depends on the material used in the manufacture of the thermoelectric device, the temperature gradient ∇T, which occurs given the temperature of T_{PVP} and T_c and electric field E_v, which is a product of the electric potential gradient ∇V. This set of Eqs. (16), (17) and (18) determine the output current and voltage of the each TEG.

$$J = \sigma_e E_v + J_e, \tag{16}$$

$$E_v = -\nabla V, \tag{17}$$

where:

$$J_e = -\sigma_e S \nabla T. \tag{18}$$

2.4. TEG configuration

To ascertain the optimal number of thermoelectric devices, arrays comprising varying quantities of TEGs, spanning from five to seventy elements, were subjected to analysis. The surface area with which TEG comes into contact is the result of dividing the total panel area by the number of TEGs. An example of this distribution is shown in Fig. 3. The conversion efficiency assumed for these configurations was 5.4% for the TEGs [33], under AM 1.5 illumination conditions. This analysis was undertaken to elucidate the individual and collective generation capabilities of the devices.

2.5. Generation of PV-TGS

Once the simulations had been validated, the electrical power obtained per unit of surface area was standardized. Consequently, a surface area of 1 m^2 and a conversion efficiency of PV panel 26.7% were considered as a reference for the remainder of the simulations [34]. The electrical power produced by the system was regarded as the summation of the generation of the photovoltaic panel and the production of the thermoelectric generator array for various values of G.

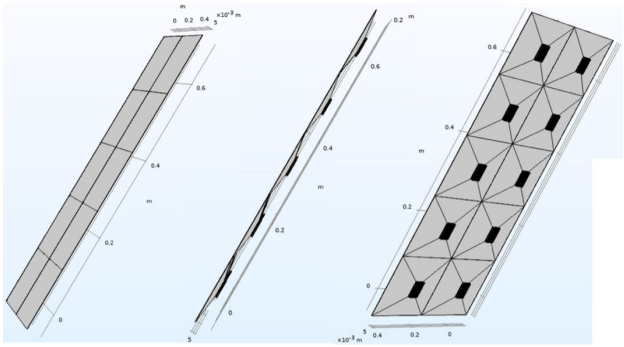

FIGURE 3. Example of distribution of the TEGs (10) in the rear section of the PV panel.

2.6. Validation of PV-TGS simulations

A comparative analysis is conducted, comparing the outcomes of this research with previously published experimental and theoretical studies, including those conducted by [35-39]. The comparison was conducted to analyze the following key factors: the number of thermoelectric generators employed, the temperature difference at which they operate, the power output of each TEG, and the overall increase in electrical power generated by the system, encompassing both thermoelectric and photovoltaic components.

3. Results and analysis

3.1. PV panel generation

The power values obtained by the panel simulation, as described in Sec. 2.1.5, are presented in Fig. 4. As anticipated, the power output increases with the incident radiation, reaching a peak of 86.25 W at 2000 W/m^2. Consequently, the operating temperature also rises to 87.50°C, resulting in a decrease in the open circuit voltage V_{OC} from 21.5 to 16.26 V.

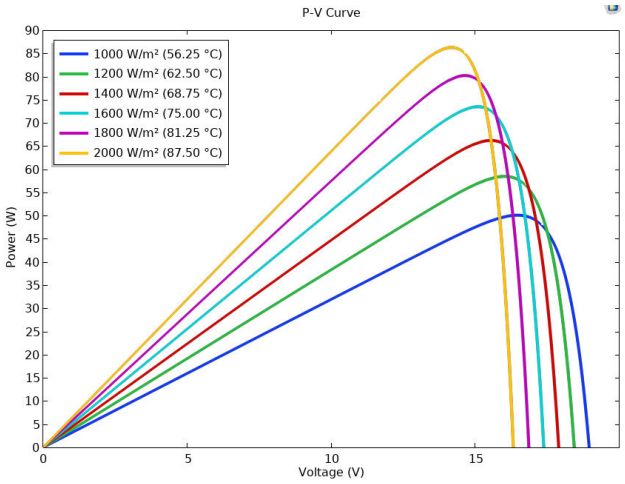

FIGURE 4. A comparative analysis of the electrical power output generated by a photovoltaic panel at varying G values, conducted through computational simulations.

TABLE II. A comparative analysis of previously reported simulations of photovoltaic cells and panels with the model generated by this research.

Reference	Power	Power obteined in this research W	Difference(%)
[14]	60.00	59.99	-0.017
[15]	250.00	245.66	-1.740
[18]	1.93×10^{-3}	1.97×10^{-3}	+1.780

TABLE III. A comparative analysis of previously reported simulations of photovoltaic cells and panels with the model generated by this research.

Temperature difference °C	Kryotherm V	Simulation V	Percent difference (%)
170	7.50	7.34	-2.45
150	6.60	6.45	-2.27
120	5.35	5.20	-2.80

The observed curves accurately depict the well-established and previously documented behavior of this energy conversion process, indicating the representativeness of the simulation. This phenomenon arises from the reduction in the energy gap between energy levels as a result of temperature increase. Consequently, the valence band gradually approaches the conduction band, leading to a decrease in the potential energy necessary to attain a specific energy level. This reduction in potential energy is disadvantageous at the macroscopic level, resulting in a lower voltage, as reported in previous research such as that conducted by [9,22,40-41].

3.2. Validation of PV panel simulations

The comparison between previous research and the results of this research is presented in Table II. It is evident that the output power values exhibit a range of -0.017 to +1.78%, indicating that the model is suitable for simulating photovoltaic cells and panels. This suggests that the model can be utilized for the design and planning of commercial and research photovoltaic and/or hybrid systems.

3.3. Simulation TEGs

Figures 5 and 6 illustrate the heat transfer and electrical potential differences, respectively, resulting from a temperature difference of 170°C. Furthermore, Table III compares the simulation results with the manufacturer's characterization data, which spans a voltage output range of -2.27% to -2.8%. This fluctuation could be attributed to the uncertainty regarding the precise concentration of dopants in the thermoelectric material, which consequently impacts the electrical measurements. Given this range, the simulation serves as a suitable approximation of the actual phenomenon and can be employed for the simulation of the PV-TGS.

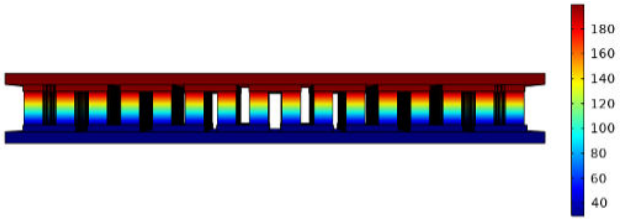

FIGURE 5. Temperature gradients between sections of the 170°C TEG.

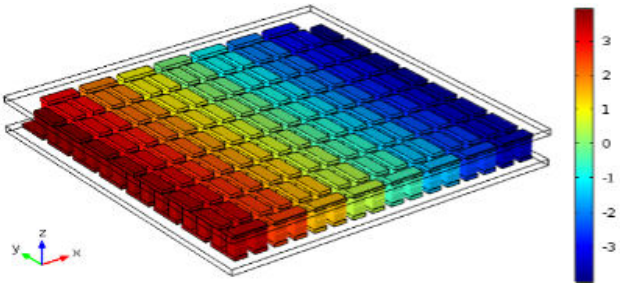

FIGURE 6. Potential difference between the TEG terminals with temperature gradient = 170°C.

3.4. TEGs Configuration

Based on the data obtained from the simulations, the power generated by each array is presented in Fig. 7. It is evident that the power generated by each array is proportional to the temperature in the cold section. This is because as the T_c is reduced, the temperature difference between the two sides of the TEGs increases, resulting in a greater heat flow. Consequently, this heat flow translates into a higher conversion rate, due to an increase in the efficiency of TEGs. However, it is important to note that, under the simulated gradients, the operating temperature of the photovoltaic panel was not

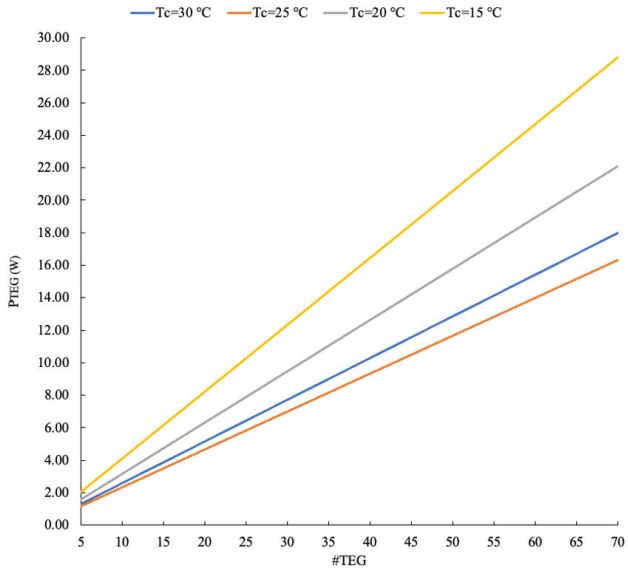

FIGURE 7. Power produced as a function of T_c according to the number of TEGs used in each array.

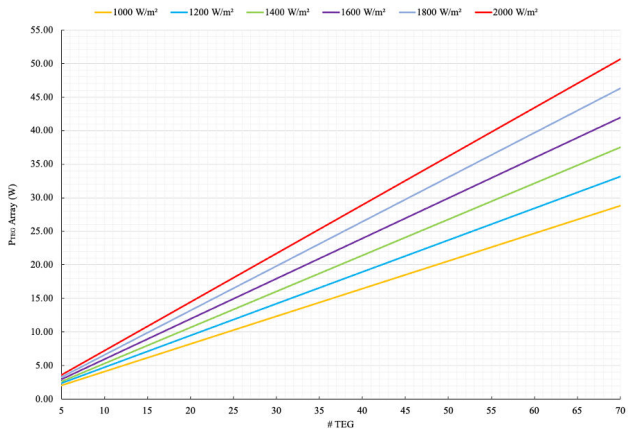

FIGURE 8. Power produced by each TEG configuration under different G conditions at $T_c = 15°$C.

significantly reduced. Therefore, the thermoelectric devices primarily function as an additional source of energy conversion rather than as a cooling system. The latter is most likely attributed to the relatively small temperature difference between the two sections of the TEGs, which fluctuates between 41.25 and 62.50°C. This gradient significantly deviates from the 170°C recommended by the manufacturer to optimize performance. However, it is noteworthy that with adequate cooling, the output power can be elevated from 16.33 W to 28.82 W, resulting in a 76.48% enhancement compared to the configuration employing the highest number of TEGs. This ratio, considering the prevailing generational trend, appears to be consistent across all configurations.

Figure 8 presents a comparative analysis of the power generated by each TEGs array at $T_c = 15°$C (the optimal performance point) among the multiple arrays under identical irradiance conditions as those simulated for the photovoltaic panel. It is evident that, as the temperature of the photovoltaic panel increases, the TEG power also rises due to the enhanced heat flux, as previously discussed. Consequently, this power exhibits a linear relationship with the number of elements. However, an increasing number of TEGs leads to higher generation costs. Therefore, it is crucial to determine the optimal number of elements that maintains a favorable cost-per-watt generated ratio. As depicted in Fig. 7, the generation behavior of the TEGs exhibits a linear pattern. Conversely, when analyzing the power output of the TEGs individually as a function of the incident radiation G in the system (Fig. 9), it is observed that the conversion efficiency η_{TEG} diminishes, following the trend outlined in Eq. (19). This observation facilitates the prediction of the generation capacity of a TEGs array, provided that the incident radiation intensity on the panel is known and subsequently multiplied by the number of elements.

$$\eta_{\text{TEG}}(G) = -2.29 \times 10^{-12} G^3 + 1.37 \times 10^{-8} G^2 - 3 \times 10^{-5} G + 5.97 \times 10^{-2}. \quad (19)$$

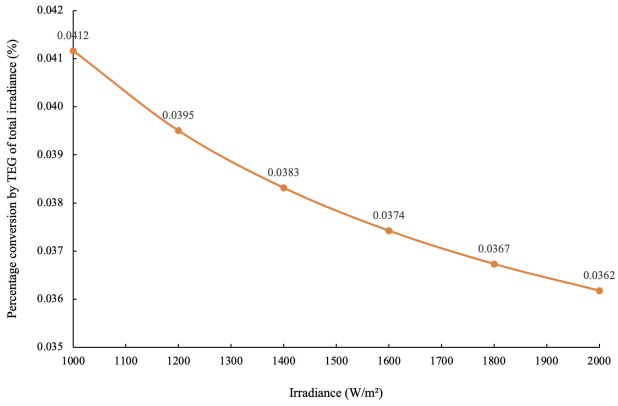

FIGURE 9. Conversion efficiency of TEGs as a function of incident solar radiation on the PV panel surface.

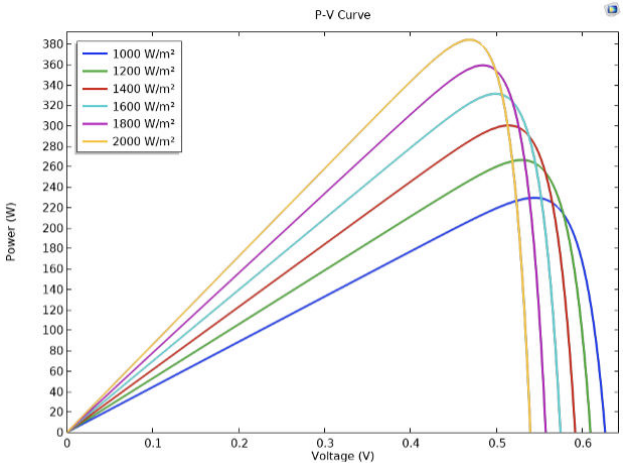

FIGURE 10. Comparison of the power generated per m^2 at different G values of the mSi panel.

3.5. Generation of PV-TGS

Finally, Fig. 10 illustrates the power generated per square meter by the photovoltaic panel under various G conditions. This curve reflects the behavior observed and described in Fig. 4. Conversely, Fig. 11 presents the total power obtained by the different PV-TGS configurations. It is evident that, as the incident radiation increases, both the panel and the TEGs array generate more power due to the irradiance and temperature difference, respectively. However, this increase is not proportional. Each time the radiation intensity increases, the power difference between the previous configuration and the subsequent one (with higher G) decreases. This is due to the aforementioned: as the increase in power increases proportionally with the increase in radiation, the voltage does not decrease proportionally but rather depends on the temperature coefficient, which depends not only on the base material, in this case silicon, but also on the amount of dopants, the production quality of the material, and the exposure and operation period of the panel, without omitting the discussion

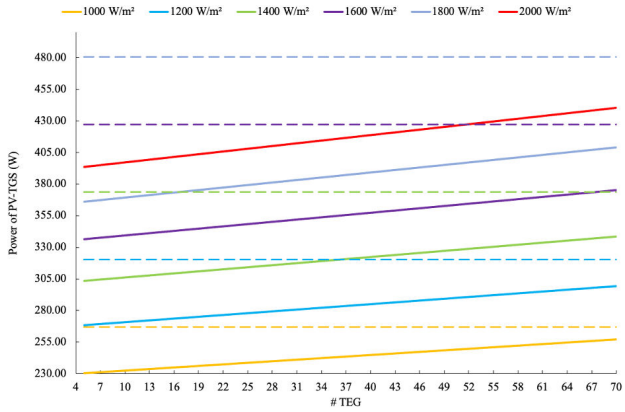

FIGURE 11. Comparison of the power generated per m^2 at different G values of the PV-TGS with $T_c = 15°C$ and its PV equivalent at 25°C (dotted lines).

on the decline in TEG conversion efficiency due to incident radiation. In comparison with the power achievable at 25°C by the PV panel (dotted lines), the same Fig. 11 demonstrates several equivalent circuits (PV panel + TEGs array) that can provide the same electrical power. These circuits are detailed in Table IV. According to these circuits, increasing the operating temperature may necessitate a smaller number of thermoelectric devices or improved cooling of the PV panel, despite the aforementioned considerations. This is particularly significant because, in most cases, it is more feasible to enhance the concentrated radiation than to reduce the temperature through cooling processes. In such cases, this often involves either supplying additional energy or consuming it directly from the PV system, thereby reducing the overall usable power.

Given the comprehensive data analysis, the system power calculation can be streamlined using the equation derived from the graph depicted in Fig. 11, as presented in Eq. (20) as a steady-state solution. This equation incorporates the slope, which represents the individual power output of each TEG, directly proportional to the irradiance conditions under which it operates. Where P_{PV-TGS} is the power of the PV-TGS, $P_{TEG}(T)$ is the power produced by a TEG as a function of temperature. (Additionally, the value can be calculated using Eq. (16), n_{TEG} is the number of TEGs in the array and $P_{PV}(T)$ is the power of the photovoltaic panel depending on the operating temperature.

$$P_{PV-TGS} = P_{TEG}(T)\, n_{TEG} + P_{PV}(T)\,. \qquad (20)$$

To obtain the values of $P_{PV}(T)$ and $P_{TEG}(T)$ it is possible to use the values provided by the manufacturer in order to facilitate their calculation as shown in Eqs. (21) and (22), where R_T is the thermal resistance of the TEG, where P_{PV} is the power produced by the PV panel under ideal operating conditions (according to the manufacturer), $T(G)$ is the temperature as a function of irradiance, T_{amb} is the ambient temperature, and C_T is the coefficient of power loss due to temperature. For its part, the $T(G)$ can be obtained using

TABLE IV. Comparison of equivalent circuits (PV Panel + TEGs Array) that can generate power equivalent to the PV panel alone at 25°C (AM 1.5 conditions).

Power W	Equivalent circuit	
267.00 (1000 W/m^2)	$\Delta T = 47.50$°C (1200 W/m^2) $+5TEGs$	-
320.40 (1200 W/m^2)	$\Delta T = 53.75$°C (1400 W/m^2) $+37TEGs$	-
373.80 (1400 W/m^2)	$\Delta T = 66.25$°C (1800 W/m^2) $+18TEGs$	$\Delta T = 60.16$°C (1600 W/m^2) $+67TEGs$
427.20 (1600 W/m^2)	$\Delta T = 72.50$°C (2000 W/m^2) $+52TEGs$	-

TABLE V. Comparative table of generation and performance increase in different hybrid systems.

Reference	$TEGs$	ΔT(°C)	Power produced by each TEG (W)	Increased system power (%)	Increased calculated in this research (%)
[35][a]	4	12.23	-	5.07	0.576
[36][b]	1	23.86	0.31	38.27	28.85
[37][c]	16	9.61-16.60	0.045-0.065	14.82-40.54	20.43
[38][d]	1	8-18	0.50	5.00	4.80
[39][e]	4-5	5-25	74.60	13.37	12.74

[a]Used in Peltier mode and with fans, [b]Used aluminum heat sink and solar cell of 1.12 W, [c]Used aluminum heat sink and solar cell of 5 W, [d]Using gallium arsenide (GaAs) cells and concentration and [e]With high concentration.

models such as Ross [42] or Nasrin [32]. Under thermal equilibrium conditions, $T_h = P_{PV}(T)$ and η_{TEG} is the TEG efficiency.

$$P_{TEG}(T) = \frac{T_h - T_c}{R_T}\eta_{TEG}, \tag{21}$$

$$P_{PV}(T) = P_{PV}\left[1 - ((T(G) - T_{amb}) * C_T)\right]. \tag{22}$$

Consequently, to determine the optimal number of TEGs for a specified power output, Eq. (23) can be employed, which was obtained by following the slope behavior of the number of TEGs and their generation. In the particular scenario of transitioning from a PV system to a PV-TGS configuration, with n_{TEG_0} initially set to 0.

$$P - P_0 = P_{TEG}(n_{TEG} - n_{TEG_0}), \tag{23}$$

where P is the desired power, P_0 is the starting power, n_{TEG} is the appropriate number of TEGs to achieve the desired power, and n_{TEG_0} is the starting number of TEGs.

3.6. Validation of PV-TGS simulations

The results of the comparison are shown below in Table V. It can be seen that the conversion increase values determined by simulating the test conditions, although not exactly the same, belong to the same order of magnitude, with the exception of the results obtained by [35]. This is attributed to the device's usage, as it operates in Peltier mode rather than employing the Seebeck effect. According to the results, this approach may be more effective in lowering the panel's temperature. However, it necessitates the provision of electrical energy, whether additional or generated by the system itself. This can be counterproductive if the system includes components such as circulation pumps or fans. Similarly, it is evident that the majority of previously published works employ various cooling methods. Notably, only those requiring heat sinks or air as the cooling fluid do not necessitate additional energy for this purpose. Although this work did not explicitly consider the cooling techniques employed in the cold section, the application of the derived mathematical models remains appropriate. This is because the temperature difference between the TEG sections is the primary factor relevant to the model, irrespective of the method used to achieve it. Consequently, this approach facilitates the standardization of equation usage across diverse solar hybrid system configurations.

4. Conclusions

Based on the results obtained, the following conclusions are drawn: The direct coupling of TEGs to PV panels presents a viable alternative, particularly when a high temperature difference is achievable. This difference can be achieved through an adequate cooling system or by increasing the irradiance concentration. The latter approach is generally more advantageous as it can be achieved using concentrating mirrors or reinforcing reflectors, technologies that have already been explored and researched. These technologies offer low-cost alternatives compared to most cooling systems that necessitate a power source. This observation is further corroborated by noting that, in each circuit with an equivalent, the temperature difference is only 6.25°C. Consequently, the number of TEGs required in each array can vary depending on the attainable power output. For instance, in the

case where a radiation incident of 1400 W/m^2 can generate 373.80 W, the number of TEGs can be approximately 3.72 times greater (from 18 to 67 TEGs). On the other hand, it is widely known that the operating temperature of the cells used for these panels is between 25 and 45°C. However, increasing the incident radiation will affect this temperature range. As observed in the results of this research, temperatures range between 56.25 and 87.50°C, which exceed the aforementioned temperature and consequently reduce the efficiency of the system. Therefore, to further enhance the usable power of this type of system, TEGs must improve their conversion efficiency. This would enable them to function not only as a secondary form of energy transformation but also as a cooling device for the photovoltaic section, thereby augmenting the overall performance of the system. Finally, the development of a predictive model for determining the optimal number of TEGs in PV-TGS Eqs. (19) and (23) designs significantly facilitate the design process of these energy systems. This model enables the exploration of diverse configurations and potential applications, including the selection of appropriate materials for both TEGs and PV panels.

Acknowledgments

We extend our sincere gratitude to the Secretariat of Science, Humanities, Technology and Innovation (SECIHTI) for the scholarship awarded to Demetrio Fuentes Hernández, whose CVU is 789052, to support his doctoral research and studies endeavors.

1. R. Sangi, M. Amidpour, and B. Hosseinizadeh, Modeling and numerical simulation of solar chimney power plants, *Solar Energy*, **85** (2011) 829, https://doi.org/10.1016/j.solener.2011.01.011
2. A. Starowicz, P. Rusanowska, and M. Zieliński, Photovoltaic cell - the history of invention - review, 2023, Mineral and Energy Economy Research Institute of the Polish Academy of Sciences. https://doi.org/10.33223/epj/161290
3. W. Shockley and H. J. Queisser, Detailed balance limit of efficiency of p-n junction solar cells, *J Appl Phys*, **32** (1961) 510, https://doi.org/10.1063/1.1736034
4. S. S. Indira, C. A. Vaithilingam, and R. Sivasubramanian, Performance Evaluation of a Hybrid Photovoltaic/Thermoelectric Generator System under Non-Tracking and Tracking Condition, 14th EURECA 2020 - International Engineering and Computing Research Conference "Shaping the Future through Multidisciplinary Research", Selangor, Malaysia, 2021, p. 15, https://doi.org/10.1051/matecconf/202133502009
5. M. Asvad, M. Gorji, and A. Mahdavi, Performance analysis of a solar module with different reflectors and cooling flow fields, *Appl Therm Eng*, **219** (2023) 119469, https://doi.org/10.1016/j.applthermaleng.2022.119469.
6. D. F. Hernández *et al*., Computational Simulation in Solar Energy: Effect of Passive Cooling in the Generation of Photovoltaic Cells in Pachuca de Soto, Mexico, Revista de Gestão Social e Ambiental, **18** (2024) e09793, https://doi.org/10.24857/rgsa.v18n11-263.
7. R. Baccoli *et al*., A comprehensive optimization model for flat solar collector coupled with a flat booster bottom reflector based on an exact finite length simulation model, *Energy Convers Manag*, **164** (2018) 482, https://doi.org/10.1016/j.enconman.2018.02.091
8. D. Fuentes Hernández, M. Vargas Ramírez, F. Legorreta García, and E. A. Chávez Urbiola, Simulación computacional de generadores termoeléctricos de telururo de bismuto, (2022). https://www.uaeh.edu.mx/xv-encuentro-investigacion-aactym/memorias/docs/art20.pdf
9. M. del R. Morales Díaz, E. Rosendo Andrés, R. Galeazzi Isasmendi, and H. Pérez Ladrón de Guevara, Modelado y simulación de celdas solares transparentes a base de la heterounión n-TiO2/p-NiO., Benemerita Universidad Autónoma de Puebla, Puebla de Zaragoza, México, (2021). https://repositorioinstitucional.buap.mx/server/api/core/bitstreams/a32c096a-596b-48db-8500-a9b2d07391fc/content
10. D. Fuentes-Hernández, R. Pérez-Vite, F. Legorreta-García, M. Vargas-Ramírez, and E. A. Chávez-Urbiola, Simulación computacional del desempeño de un sistema fotovoltaico acoplando generadores termoeléctricos y reflectores difusos de refuerzo, *Pädi Boletín Científico de Ciencias Básicas e Ingenierías del ICBI*, **8** (2020) 128, https://doi.org/10.29057/icbi.v8iespecial.6335
11. R. D. Judkoff, Validation of Building Energy Analysis Simulation Programs at the Solar Energy Research Institute, *Energy Build*, **10** (1988) 221, https://doi.org/10.1016/0378-7788(88)90008-4.
12. J. A. Gow and C. D. Manning, Development of a model for photovoltaic arrays suitable for use in simulation studies of solar energy conversion systems, 1996 Sixth International Conference on Power Electronics and Variable Speed Drives (Conf. Publ. No. 429), Nottingham, UK, 1996, pp. 69-74, https://doi.org/10.1049/cp:19960890
13. R. M. da Silva and J. L. M. Fernandes, Hybrid photovoltaic/thermal (PV/T) solar systems simulation with Simulink/Matlab, *Solar Energy*, **84** (2010) 1985, https://doi.org/10.1016/j.solener.2010.10.004
14. C. Qi and Z. Ming, Photovoltaic Module Simulink Model for a Stand-alone PV System, *Phys Procedia*, **24** (2012) 94, https://doi.org/10.1016/j.phpro.2012.02.015
15. E. E. Granda-Gutiérrez, J. C. Díaz-Guillén, M. A. Jiménez, and M. Osorio, Modelado y Simulación de Celdas y Paneles Solares, *Congr. Int. Ing. Electrón. Mem. Electro*, Chihuahua, Chih. México, 2013, pp. 17-22, https://doi.org/10.13140/2.1.4192.8968

16. A. Abdulameer, A. Al-Khazzar, and A. A. Abood, A comprehensive solar angles simulation and calculation using Matlab, *International Journal of Energy and Environment*, **6** (2015) 367, https://api.semanticscholar.org/CorpusID:62925818.
17. Y. Bouzelata, E. Kurt, R. Chenni, and N. Altin, Design and simulation of a unified power quality conditioner fed by solar energy, *Int J Hydrogen Energy*, **40** (2015) 15267, https://doi.org/10.1016/j.ijhydene.2015.02.077
18. M. Sánchez Fraile and F. Naranjo Vega, Desarrollo de una herramienta para el modelado del comportamiento eléctrico de células solares, degree thesis, Escuela Politécnica Superior, Universidad de Alcalá, Alcalá de Henares, España (2019).
19. K. W. Qadir, A simulation study on the effect of size gold nanoparticles on broadband light absorption in dye-sensitised solar cells, *Rev. Mex. Fis.* **67** (2021) 509, https://doi.org/10.31349/RevMexFis.67.509.
20. M. A. Qasim, N. T. Alwan, S. Praveenkumar, V. I. Velkin, and E. B. Agyekum, A new maximum power point tracking technique for thermoelectric generator modules, *Inventions*, **6** 2021, https://doi.org/10.3390/inventions6040088
21. M. S. Yagoub and M. Adnane, Numerical study of P3HT-based hybrid solid-state quantum dot solar cellswith CdS quantum dots employing different metal oxides using SCAPS-1D, *Rev. Mex. Fis.* **70** (2024) 1, https://doi.org/10.31349/RevMexFis.70.061001
22. K. Ouassoul, A. El Kenz, M. Loulidi, A. Benyoussef, and M. Azzouz, Prediction of the photovoltaic performance of the lead-free layered Ruddlesden-Popper organic-inorganic perovskite (CH3NH3)2GeI4, *Rev. Mex. Fis.* **70** (2024) 1, https://doi.org/10.31349/revmexfis.70.040502
23. P. Khatri, N. P. Adhikari, and P. Ghosh, Thermoelectric properties of low thermal conductivity half Heuslers TiXPb (X = Ni, Pd, Pt): A first principles investigation, *Comput Mater Sci*, **244** (2024) 113250, https://doi.org/10.1016/j.commatsci.2024.113250.
24. Comsol Multiphysics, COMSOL Multiphysics Reference Manual, (1998). Available: www.comsol.com/blogs
25. COMSOL Multiphysics, Si Solar Cell 1D, 2019. Available: www.comsol.com/trademarks
26. American Society for Testing and Materials (ASTM), ASTM G173-03: Standard Tables for Reference Solar Spectral Irradiances: Direct Normal and Hemispherical on 37° Tilted Surface, West Conshohocken, Pennsylvania, USA, 2021, pp. 20 https://store.astm.org/g0173-03.html.
27. J. F. Shackelford and M. P. Martín, Introducción a la ciencia de materiales, 6th ed. (Pearson Educación, S.A., Prentice Hall, Madrid, Spain, 2005), pp. 872.
28. L. Wang and J. Yu, Principles of photocatalysis, in *Interface Science and Technology*, **35** (2023) 1, https://doi.org/10.1016/B978-0-443-18786-5.00002-0.
29. Solartec, Solartec Energía Renovable S.A de C.V., (Datasheet, 2019).
30. The National Laboratory of the Rockies, Reference Air Mass 1.5 Spectra, The American Society for Testing and Materials (ASTM) G-173 spectra represent terrestrial solar spectral irradiance on a surface of specified orientation under one and only one set of specified atmospheric conditions, National Renewable Energy Laboratory (NREL), Denver, Colorado, USA, 2025, https://www.nrel.gov/grid/solar-resource/spectra-am1.5
31. A. R. West, Solid State Chemistry and its Applications, 2nd ed., ohn Wiley & Sons Ltd, The Atrium, Southern Gate, Chichester, West Sussex, United Kingdom, 2014, pp. 382-389.
32. R. Nasrin, M. Hasanuzzaman, and N. A. Rahim, Effect of high irradiation on photovoltaic power and energy, *Int. J. Energy Res.* **42** (2018) 1115, https://doi.org/10.1002/er.3907
33. Kryotherm, Specification of Generating Thermoelectric Modules TGM-127-1.4-2.5, 2020.
34. M. A. Green *et al*., Solar cell efficiency tables (Version 60), *Progress in Photovoltaics: Research and Applications*, **30** (2022) 687, https://doi.org/10.1002/pip.3595
35. S. Praveenkumar *et al*., Experimental assessment of thermoelectric cooling on the efficiency of PV module, *International Journal of Renewable Energy Research*, **12** (2022) 1670, https://doi.org/10.20508/ijrer.v12i3.13087.g8553
36. B. R. Utomo, A. Sulistyanto, T. W. B. Riyadi, and A. T. Wijayanta, Enhanced Performance of Combined Photovoltaic-Thermoelectric Generator and Heat Sink Panels with a Dual-Axis Tracking System, *Energies*, **16** (2023) 6, https://doi.org/10.3390/en16062658
37. N. Calderón-Henao *et al*., Numerical-experimental performance assessment of a non-concentrating solar thermoelectric generator (STEG) operating in the Southern Hemisphere, *Energies* **13** (2020) 10, https://doi.org/10.3390/en13102666.
38. A. M. Alajlan, S. Dang, and Q. Gan, Enhanced nighttime power generation and photovoltaic cooling in photovoltaic-thermoelectric hybrid systems, *Energy Conversion and Management.* **22** (2024) 100580, https://doi.org/10.1016/j.ecmx.2024.100580
39. Z. He, M. Yang, L. Wang, E. Bao, and H. Zhang, Concentrated photovoltaic thermoelectric hybrid system: An experimental and machine learning study, *Engineered Science*, **15** (2021) 47, https://doi.org/10.30919/es8d440.
40. N. Rosario, F. Rivera, M. ángel, D. Ramírez, and R. Ramírez Bon, Medición de la eficiencia energética de los paneles solares de silicio. Centro De Investigación En Materiales Avanzados, 2016. https://cimav.repositorioinstitucional.mx/jspui/handle/1004/215
41. M. A. Khan, B. Ko, E. A. Nyari, S. E. Park, and H. J. Kim, Performance evaluation of photovoltaic solar system with different cooling methods and a Bi-reflector PV system (BRPVS): An experimental study and comparative analysis, *Energies*, **10** (2017) 6, https://doi.org/10.3390/en10060826.
42. K. Ouassoul, A. El Kenz, M. Loulidi, A. Benyoussef, and M. Azzouz, Prediction of the photovoltaic performance of the lead-free layered Ruddlesden-Popper organic-inorganic perovskite (CH3NH3)2GeI4, *Rev. Mex. Fís.* **70** (2024) 1, https://doi.org/10.31349/revmexfis.70.040502.
43. R. G. Ross, Flat-Plate photovoltaic array design optimization, in Photovoltaic Specialists Conference, 14th, San Diego, Calif, Inc. I. Institute of Electrical and Electronics Engineers, Ed., New York: Conference Record, Jan. 1980, pp. 1126-1132.